Computers and Mathematics with Applications 77 (2019) 311–322

Contents lists available at ScienceDirect

Computers and Mathematics with Applications

journal homepage: www.elsevier.com/locate/camwa

Comparison study on the different dynamics between the Allen–Cahn and the Cahn–Hilliard equations

Yibao Li [a], Darae Jeong [b], Hyundong Kim [c], Chaeyoung Lee [c], Junseok Kim [c,*]

[a] School of Mathematics and Statistics, Xi'an Jiaotong University, Xi'an 710049, China
[b] Department of Mathematics, Kangwon National University, Gangwon-do 24341, Republic of Korea
[c] Department of Mathematics, Korea University, Seoul 02841, Republic of Korea

HIGHLIGHTS

- We perform a comparison study on dynamics between the AC and CH equations.
- Linear stability analysis shows that growing and decaying modes are the same.
- The growth rates are monotonically decreasing for the AC equation.
- The growth rates for the CH equation are non-monotonic.

ARTICLE INFO

Article history:
Received 5 September 2017
Received in revised form 23 July 2018
Accepted 15 September 2018
Available online 17 October 2018

Keywords:
Allen–Cahn equation
Cahn–Hilliard equation
Linear stability analysis
Fourier spectral method
Fastest growing mode

ABSTRACT

We perform a comparison study on the different dynamics between the Allen–Cahn (AC) and the Cahn–Hilliard (CH) equations. The AC equation describes the evolution of a non-conserved order field during anti-phase domain coarsening. The CH equation describes the process of phase separation of a conserved order field. The AC and the CH equations are second-order and fourth-order nonlinear parabolic partial differential equations, respectively. Linear stability analysis shows that growing and decaying modes for both the equations are the same. While the growth rates are monotonically decreasing with respect to the modes for the AC equation, the growth rates for the CH equation are increasing and then decreasing with respect to the modes. We perform various numerical tests using the Fourier spectral method to highlight the different evolutionary dynamics between the AC and the CH equations.

1. Introduction

The Allen–Cahn (AC) equation [1], which is a second-order nonlinear parabolic partial differential equation, describes the evolution of a non-conserved order field during anti-phase domain coarsening:

$$\frac{\partial \phi(\mathbf{x},t)}{\partial t} = -\frac{F'(\phi(\mathbf{x},t))}{\epsilon^2} + \Delta\phi(\mathbf{x},t), \quad \mathbf{x} \in \Omega, \ t > 0, \tag{1}$$

where $\Omega \subset \mathbb{R}^d$ $(d = 1, 2, 3)$ is a domain. Here, $\phi(\mathbf{x}, t)$ is an order parameter, $F(\phi) = 0.25(\phi^2 - 1)^2$ is the free energy per unit volume, and the small constant ϵ is the gradient energy coefficient related to the interfacial energy. At the boundary,

* Corresponding author.
E-mail addresses: yibaoli@xjtu.edu.cn (Y. Li), cfdkim@korea.ac.kr (J. Kim).
URLs: http://gr.xjtu.edu.cn/web/yibaoli (Y. Li), http://math.korea.ac.kr/~cfdkim (J. Kim).

https://doi.org/10.1016/j.camwa.2018.09.034
0898-1221/

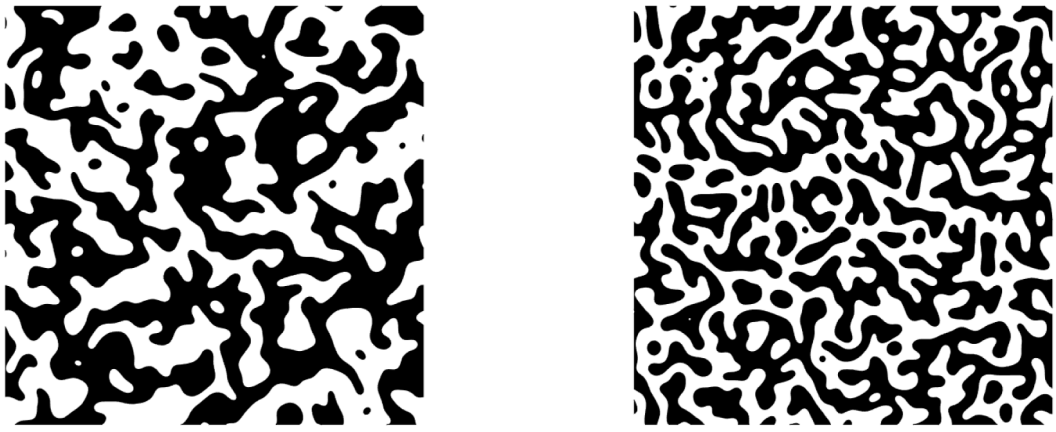

Fig. 1. Snapshots of phase separation by (a) the AC and (b) the CH equations.

we apply the periodic boundary condition. The AC equation is the L^2-gradient flow of the following total free energy

$$\mathcal{E}_{\mathrm{AC}}(\phi) := \int_{\Omega} \left(\frac{F(\phi)}{\epsilon^2} + \frac{1}{2}|\nabla\phi|^2 \right) \mathrm{d}\mathbf{x}. \tag{2}$$

Differentiating $\mathcal{E}_{\mathrm{AC}}(\phi)$ with respect to time, we obtain:

$$\begin{aligned} \frac{\mathrm{d}}{\mathrm{d}t}\mathcal{E}_{\mathrm{AC}}(\phi) &= \int_{\Omega} \left(\frac{F'(\phi)}{\epsilon^2}\phi_t + \nabla\phi \cdot \nabla\phi_t \right) \mathrm{d}\mathbf{x} \\ &= \int_{\Omega} \left(\frac{F'(\phi)}{\epsilon^2} - \Delta\phi \right) \phi_t \mathrm{d}\mathbf{x} = -\int_{\Omega} (\phi_t)^2 \mathrm{d}\mathbf{x} \leq 0. \end{aligned}$$

Therefore, the total energy is non-increasing in time. The AC equation has been widely used to describe many important problems such as image inpainting [2], two-phase incompressible fluids [3], complex dynamics of dendritic growth [4,5], mean curvature flows [6–8], and image segmentation [9,10].

The Cahn–Hilliard (CH) equation [11], which is a fourth-order nonlinear parabolic partial differential equation, describes the process of phase separation of a conserved order field as follows.

$$\frac{\partial\phi(\mathbf{x},t)}{\partial t} = \Delta\left[F'(\phi(\mathbf{x},t)) - \epsilon^2\Delta\phi(\mathbf{x},t)\right], \quad \mathbf{x}\in\Omega, \ t>0. \tag{3}$$

Here, the periodic boundary condition is considered. The CH equation is the mass-constrained gradient flow in H^{-1} of the total free energy,

$$\mathcal{E}_{\mathrm{CH}}(\phi) := \int_{\Omega} \left(F(\phi) + \frac{\epsilon^2}{2}|\nabla\phi|^2 \right) \mathrm{d}\mathbf{x}. \tag{4}$$

We also obtain the following:

$$\frac{\mathrm{d}}{\mathrm{d}t}\int_{\Omega}\phi \,\mathrm{d}\mathbf{x} = \int_{\Omega}\phi_t \,\mathrm{d}\mathbf{x} = \int_{\Omega}\Delta\left[F'(\phi) - \epsilon^2\Delta\phi\right]\mathrm{d}\mathbf{x} = 0, \tag{5}$$

$$\begin{aligned} \frac{\mathrm{d}}{\mathrm{d}t}\mathcal{E}_{\mathrm{CH}}(\phi) &= \int_{\Omega}\left(F'(\phi)\phi_t + \epsilon^2\nabla\phi\cdot\nabla\phi_t\right)\mathrm{d}\mathbf{x} \\ &= \int_{\Omega}\left(F'(\phi) - \epsilon^2\Delta\phi\right)\phi_t\mathrm{d}\mathbf{x} = -\int_{\Omega}|\nabla\left(F'(\phi) - \epsilon^2\Delta\phi\right)|^2\mathrm{d}\mathbf{x} \leq 0, \end{aligned} \tag{6}$$

As shown in Eqs. (5) and (6), the total mass is conserved and the total energy is non-increasing in time. The CH equation has been widely studied [12–15] and is widely used in applications such as topology optimization [16], multiphase incompressible fluid flows [17–20], image inpainting [21], surface reconstruction [22], diblock copolymer [23], phase separation [24], tumor growth simulation [25], and microstructures with elastic inhomogeneity [26].

In order to apply the two models to investigate interesting applications, we need to know their correct evolutionary dynamics. Both equations have similar phase separation properties, however, their dynamics are different as shown in Fig. 1. Therefore, the main purpose of this article is to investigate the different dynamics of the AC and the CH equations.

This report is organized as follows: in Section 2, we describe a numerical solution based on the Fourier spectral method for the AC and the CH equations. We present several numerical results and compare the two equations in Section 3. In Section 4, conclusions are given.

2. Numerical solution

In this section, we present a numerical solution for the AC Eq. (1) and the CH Eq. (3) using the Fourier-spectral method [27]. For the convenience of the explanation, we shall discretize the equation in two-dimensional space $\Omega = (0, L_x) \times (0, L_y)$. Let $h_x = L_x/N_x$ and $h_y = L_y/N_y$ be the spatial step sizes in the x- and y-directions, respectively. Here, N_x and N_y are positive even integers. We denote cell-centered points as $(x_m, y_n) = ((m - 0.5)h_x, (n - 0.5)h_y)$. Let ϕ^k_{mn} be an approximation of $\phi(x_m, y_n, t_k)$, where $t_k = k\Delta t$ and Δt is the temporal step. For the given data $\{\phi^k_{mn} | m = 1, \ldots, N_x$ and $n = 1, \ldots, N_y\}$, the discrete Fourier transform is defined as $\hat{\phi}^k_{pq} = \sum_{m=1}^{N_x} \sum_{n=1}^{N_y} \phi^k_{mn} e^{-i(\xi_p x_m + \eta_q y_n)}$, where $\xi_p = 2\pi p/L_x$ and $\eta_q = 2\pi q/L_y$. The inverse discrete Fourier transform is given as:

$$\phi^k_{mn} = \frac{1}{N_x N_y} \sum_{p=-N_x/2}^{N_x/2-1} \sum_{q=-N_y/2}^{N_y/2-1} \hat{\phi}^k_{pq} e^{i(\xi_p x_m + \eta_q y_n)}. \tag{7}$$

Let $\phi(x, y, k\Delta t) = \frac{1}{N_x N_y} \sum_{p=-N_x/2}^{N_x/2-1} \sum_{q=-N_y/2}^{N_y/2-1} \hat{\phi}^k_{pq} e^{i(\xi_p x + \eta_q y)}$. Then, we have

$$\Delta\phi(x, y, k\Delta t) = -\frac{1}{N_x N_y} \sum_{p=-N_x/2}^{N_x/2-1} \sum_{q=-N_y/2}^{N_y/2-1} \left(\xi_p^2 + \eta_q^2\right) \hat{\phi}^k_{pq} e^{i(\xi_p x + \eta_q y)}.$$

Now, we apply a linearly stabilized splitting scheme [28] to the AC Eq. (1) as follows.

$$\frac{\phi^{k+1}_{mn} - \phi^k_{mn}}{\Delta t} = -2\phi^{k+1}_{mn}/\epsilon^2 + \Delta\phi^{k+1}_{mn} - f(\phi^k_{mn}), \tag{8}$$

where $f(\phi) = (\phi^3 - 3\phi)/\epsilon^2$. Thus, Eq. (8) can be transformed into the discrete Fourier space as:

$$\frac{\hat{\phi}^{k+1}_{pq} - \hat{\phi}^k_{pq}}{\Delta t} = -2\hat{\phi}^{k+1}_{pq}/\epsilon^2 - \left(\xi_p^2 + \eta_q^2\right) \hat{\phi}^{k+1}_{pq} - \hat{f}^k_{pq}.$$

Therefore, we obtain the following discrete Fourier transform

$$\hat{\phi}^{k+1}_{pq} = \frac{\hat{\phi}^k_{pq} - \Delta t \hat{f}^k_{pq}}{1 + \Delta t[2/\epsilon^2 + (\xi_p^2 + \eta_q^2)^2]}.$$

Then, the updated numerical solution ϕ^{k+1}_{mn} can be computed using Eq. (7).

Next, we also apply the linearly stabilized splitting scheme [29] to the CH Eq. (3) as follows:

$$\frac{\phi^{k+1}_{mn} - \phi^k_{mn}}{\Delta t} = \Delta\left[2\phi^{k+1}_{mn} - \epsilon^2\Delta\phi^{k+1}_{mn} + f(\phi^k_{mn})\right], \tag{9}$$

where $f(\phi) = \phi^3 - 3\phi$. Thus, Eq. (9) can be transformed into the discrete Fourier space as:

$$\frac{\hat{\phi}^{k+1}_{pq} - \hat{\phi}^k_{pq}}{\Delta t} = -\left(\xi_p^2 + \eta_q^2\right)\left[2\hat{\phi}^{k+1}_{pq} + \epsilon^2\left(\xi_p^2 + \eta_q^2\right)\hat{\phi}^{k+1}_{pq} + \hat{f}^k_{pq}\right].$$

Therefore, we obtain the following discrete Fourier transform

$$\hat{\phi}^{k+1}_{pq} = \frac{\hat{\phi}^k_{pq} - (\xi_p^2 + \eta_q^2)\Delta t \hat{f}^k_{pq}}{1 + \Delta t[2(\xi_p^2 + \eta_q^2) + \epsilon^2(\xi_p^2 + \eta_q^2)^2]}.$$

Finally, the updated numerical solution ϕ^{k+1}_{mn} can be computed using Eq. (7). In general, Eyre's linearly stabilized convex splitting scheme can be written as

$$\phi^3 - \phi = f_1(\phi) - f_2(\phi), \tag{10}$$

where $f_1(\phi) = s\phi$ and $f_2(\phi) = -\phi^3 + (s + 1)\phi$ for some parameter s. We treat $f_1(\phi^{k+1})$ implicitly and $f_2(\phi^k)$ explicitly. Then, the scheme is unconditionally stable with $s \geq 2$ under the condition, $|\phi| \leq 1$. The choice $s = 2$ gives a smaller local truncation error [28].

3. Numerical experiments

3.1. Linear stability analysis

For comparison, we first perform a linear stability analysis around a spatially constant critical composition solution $\phi \equiv 0$. Linearizing the AC Eq. (1) about $\phi \equiv 0$ gives

$$\phi_t = \frac{\phi}{\epsilon^2} + \Delta\phi. \tag{11}$$

Let $\phi(\mathbf{x}, t) = \alpha(t)\prod_{i=1}^{d}\cos(k_i\pi x_i)$ for $\mathbf{x} \in \mathbb{R}^d$ where $\alpha(t)$ is an amplitude. Then, from Eq. (11), we have

$$\alpha'(t)\prod_{i=1}^{d}\cos(k_i\pi x_i) = \frac{\alpha(t)}{\epsilon^2}\prod_{i=1}^{d}\cos(k_i\pi x_i) - \sum_{i=1}^{d}(k_i\pi)^2\alpha(t)\prod_{i=1}^{d}\cos(k_i\pi x_i). \tag{12}$$

By dividing Eq. (12) by $\prod_{i=1}^{d}\cos(k_i\pi x_i)$, we obtain

$$\alpha'(t) = \left[\frac{1}{\epsilon^2} - \sum_{i=1}^{d}(k_i\pi)^2\right]\alpha(t). \tag{13}$$

The solution of the ordinary differential equation (13) is given by

$$\alpha(t) = \alpha(0)e^{\lambda_{\mathrm{AC}}t}, \tag{14}$$

where $\lambda_{\mathrm{AC}} = 1/\epsilon^2 - \sum_{i=1}^{d}(k_i\pi)^2$.

Next, linearizing the CH equation (3) about $\phi \equiv 0$ gives

$$\phi_t = \Delta(-\phi - \epsilon^2\Delta\phi). \tag{15}$$

From Eq. (15), we have

$$\begin{aligned}\alpha'(t)\prod_{i=1}^{d}\cos(k_i\pi x_i) = &\sum_{i=1}^{d}(k_i\pi)^2\alpha(t)\prod_{i=1}^{d}\cos(k_i\pi x_i)\\ &-\epsilon^2\left(\sum_{i=1}^{d}(k_i\pi)^2\right)^2\alpha(t)\prod_{i=1}^{d}\cos(k_i\pi x_i).\end{aligned} \tag{16}$$

By dividing Eq. (16) by $\prod_{i=1}^{d}\cos(k_i\pi x_i)$, we obtain

$$\alpha'(t) = \sum_{i=1}^{d}(k_i\pi)^2\left[1 - \epsilon^2\sum_{i=1}^{d}(k_i\pi)^2\right]\alpha(t). \tag{17}$$

The solution of the ordinary differential equation (17) is given by

$$\alpha(t) = \alpha(0)e^{\lambda_{\mathrm{CH}}t}, \tag{18}$$

where $\lambda_{\mathrm{CH}} = \sum_{i=1}^{d}(k_i\pi)^2[1 - \epsilon^2\sum_{i=1}^{d}(k_i\pi)^2]$. Now, we define the numerical growth rate as

$$\tilde{\lambda} = \frac{1}{T}\log\left(\frac{\|\phi^{N_t}\|_\infty}{\alpha(0)}\right). \tag{19}$$

We study linear stability analysis in one-, two- and three-dimensional spaces. In all numerical test, $\epsilon = \epsilon_m = mh/[2\sqrt{2}\tanh^{-1}(0.9)]$ means that we have approximately mh transition layers across the interfacial transition layer [30]. Unless otherwise specified, we use $N = N_x = N_y = N_z = 200$, $h = 1/N$, $\Delta t = 0.01h^2$, and $\epsilon = \epsilon_{16}$.

3.1.1. One-dimensional space

First, we perform a linear stability analysis on one-dimensional space $\Omega = (0, 1)$. The initial state is taken to be $\phi(x, 0) = 0.01\cos(k\pi(x - 0.5h))$, where k is a positive even integer less than or equal to 20. Here, we shift the cosine function by a half grid size so that we have the maximum value at the grid point. Let $\tilde{\lambda}_{\mathrm{AC}}$(circle marker), λ_{AC}(solid line) be the numerical and analytic growth rates of the AC equation, respectively.

Let $\tilde{\lambda}_{\mathrm{CH}}$(square marker), λ_{CH}(dashed lines) be the numerical and analytic growth rates of the CH equation, respectively. In Fig. 2, the numerical and analytic growth rate values for different wave numbers ($k = 2, 4, \ldots, 20$) are shown and they are in good agreement with each other. Here, $T = 1000\Delta t$ and $\alpha(0) = 0.01$ are used.

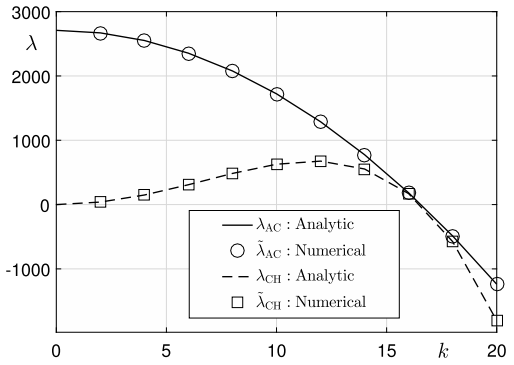

Fig. 2. Numerical and analytic growth rates for different wave numbers ($k = 2, 4, \ldots, 20$) in one-dimensional space.

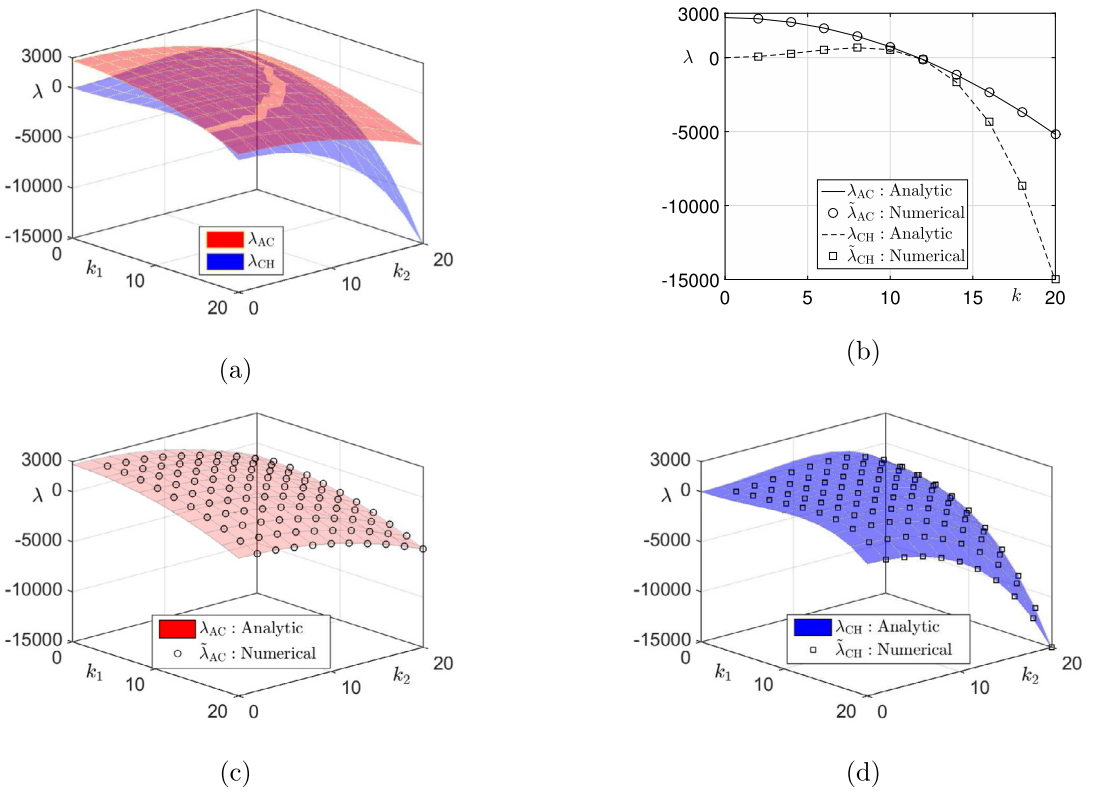

Fig. 3. (a) Analytic growth rates for the linearized AC and the CH equations. (b) Numerical and analytic growth rates for different wave numbers ($k_1 = k_2 = 2, 4, \ldots, 20$). Numerical and exact growth rates for (c) the AC and (d) the CH equations . (For interpretation of the references to color in this figure legend, the reader is referred to the web version of this article.)

3.1.2. Two-dimensional space

In the computational domain $\Omega = (0, 1) \times (0, 1)$, we investigate the linear stability of the AC and CH equations. The initial condition is set to $\phi(x, y, 0) = 0.01 \cos(k_1\pi(x - 0.5h)) \cos(k_2\pi(y - 0.5h))$, where k_1 and k_2 are positive even integers less than or equal to 20. Here, $T = 1000\Delta t$ and $\alpha(0) = 0.01$ are used.

In Fig. 3(a), the analytic growth rates derived from the linearized AC and the CH equations are represented by red and blue surfaces, respectively. In Fig. 3(b), we show the analytic and numerical growth rates for the AC and the CH equations when $k_1 = k_2 = 2, 4, \ldots, 20$, respectively. Additionally, we can observe the growth rates of the numerical solutions by the AC (circle marker) and the CH (square marker) equations in Fig. 3(c) and (d), respectively. Similar to the results for the one-dimensional space, numerical and analytic results for both the AC and the CH equations are in good agreement with each other.

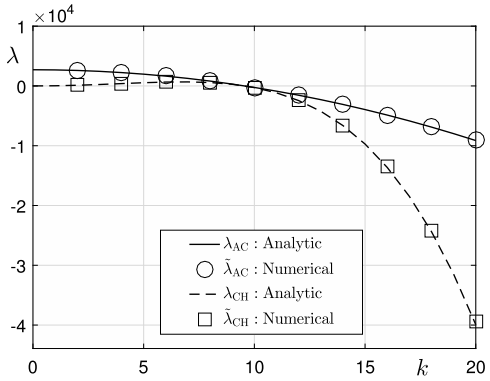

Fig. 4. Numerical and analytic growth rates for different wave numbers ($k = k_1 = k_2 = k_3 = 2, 4, \ldots, 20$) for three-dimensional space.

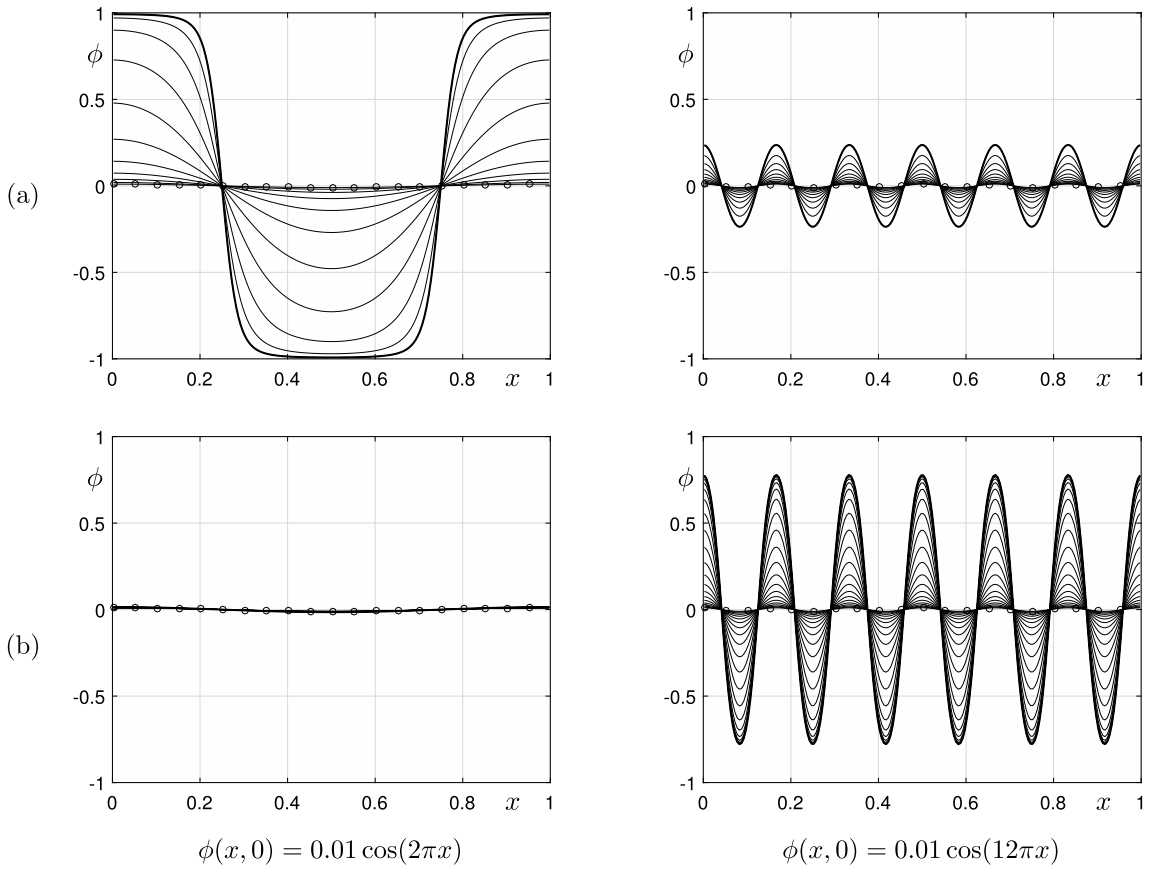

Fig. 5. Temporal evolution of (a) the AC and (b) the CH equations when the initial condition is set to $\phi(x, 0) = 0.01\cos(2\pi x)$ and $\phi(x, 0) = 0.01\cos(12\pi x)$.

3.1.3. Three-dimensional space

For three-dimensional space $\Omega = (0, 1) \times (0, 1) \times (0, 1)$, we implement the linear stability test with $\phi(x, y, z, 0) = 0.01\cos(k_1\pi(x - 0.5h))\cos(k_2\pi(y - 0.5h))\cos(k_3\pi(z - 0.5h))$, where k_1, k_2 and k_3 are positive integers less than or equal to 20. Here, $T = 100\Delta t$ and $\alpha(0) = 0.01$ are used.

To compare the growth rates for the AC and the CH equations, we illustrate the analytic and numerical growth rates and their relative absolute error when the initial mode k_1, k_2, and k_3 are the same as k. Here, we define the relative absolute error $E = |(\tilde{\lambda} - \lambda)/\lambda|$, where λ and $\tilde{\lambda}$ represents the analytic and numerical values, respectively. As shown in Table 1, the fastest growth modes of the AC and the CH equations are $k = 2$ and $k = 6$, respectively.

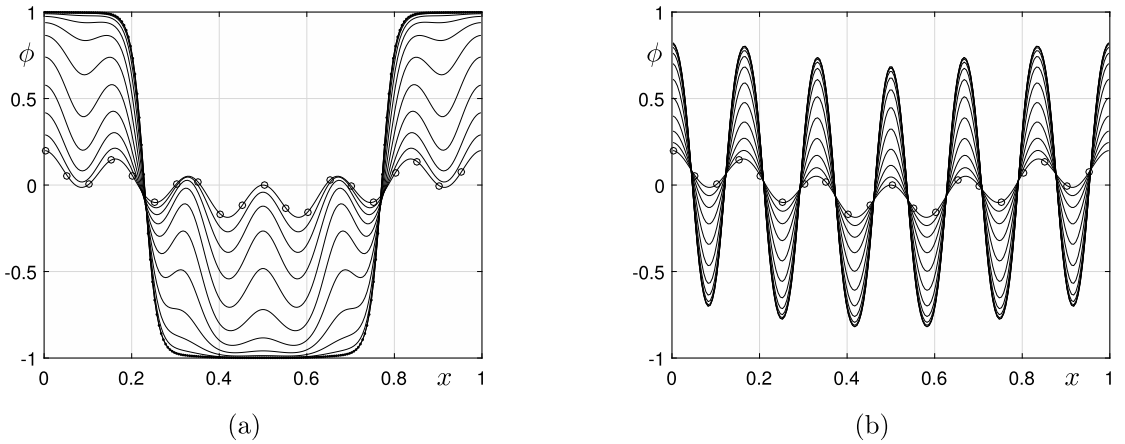

Fig. 6. Temporal evolution of (a) the AC and (b) the CH equations with the initial condition $\phi(x, 0) = 0.01[\cos(2\pi x) + \cos(12\pi x)]$.

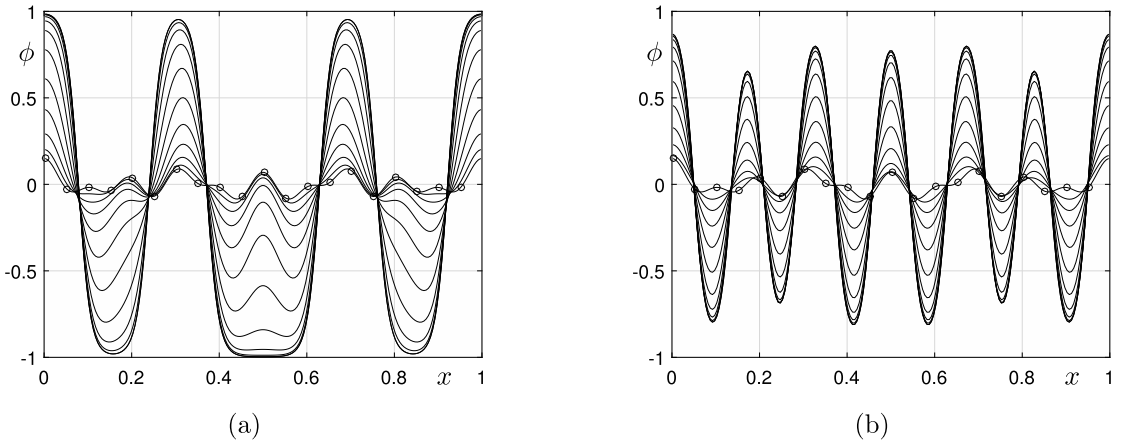

Fig. 7. Temporal evolution of (a) the AC and (b) the CH equations with the initial condition $\phi(x, 0) = 0.05\text{rand}(x)$. Here, rand$(x)$ denotes the random number between -1 and 1.

Table 1
Comparison of analytic, numerical growth rates, and their relative absolute error of the AC and the CH equations in three-dimensional space.

k	λ_{AC}	$\tilde{\lambda}_{AC}$	E_{AC}	λ_{CH}	$\tilde{\lambda}_{CH}$	E_{CH}
2	2585.9	2590.9	0.00191	113.2	113.3	0.00409
4	2231.2	2235.5	0.00195	390.6	390.9	0.00070
6	1640.0	1643.4	0.00203	645.8	646.6	0.00110
8	812.5	814.3	0.00223	568.6	569.6	0.00176
10	−251.2	−251.6	0.00141	−274.5	−275.0	0.00161
12	−1551.0	−1554.4	0.00215	−2437.7	−2446.2	0.00344
14	−3086.6	−3094.0	0.00239	−6593.4	−6627.5	0.00514
16	−4857.8	−4870.6	0.00262	−13526.7	−13626.5	0.00733
18	−6864.1	−6884.0	0.00288	−24128.3	−24375.3	0.01013
20	−9105.4	−9134.2	0.00316	−39383.8	−39929.9	0.01368

Fig. 4 shows the numerical and analytic growth rates for different wave numbers $k = k_1 = k_2 = k_3 = 2, 4, \cdots, 20$. Similar to the previous tests, it can be observed that numerical and analytic results for both the AC and the CH equations are in good agreement with each other.

The fastest growth rates of the AC equation for $1D$, $2D$, and $3D$ are the same, whereas those of the CH equation are different. The growth rates of the AC equation are $\lambda_{AC} = 1/\epsilon^2 - \sum_{i=1}^{d}(k_i\pi)^2$ for $d = 1,\ 2$, and 3, which are monotonically decreasing for all dimensions. Therefore, the maximum is $1/\epsilon^2$ for all dimensions. Whereas, those of the CH equations are $\lambda_{CH} = \sum_{i=1}^{d}(k_i\pi)^2[1 - \epsilon^2 \sum_{i=1}^{d}(k_i\pi)^2]$ for $d = 1,\ 2$, and 3, which have different minimum values depending on the dimensions.

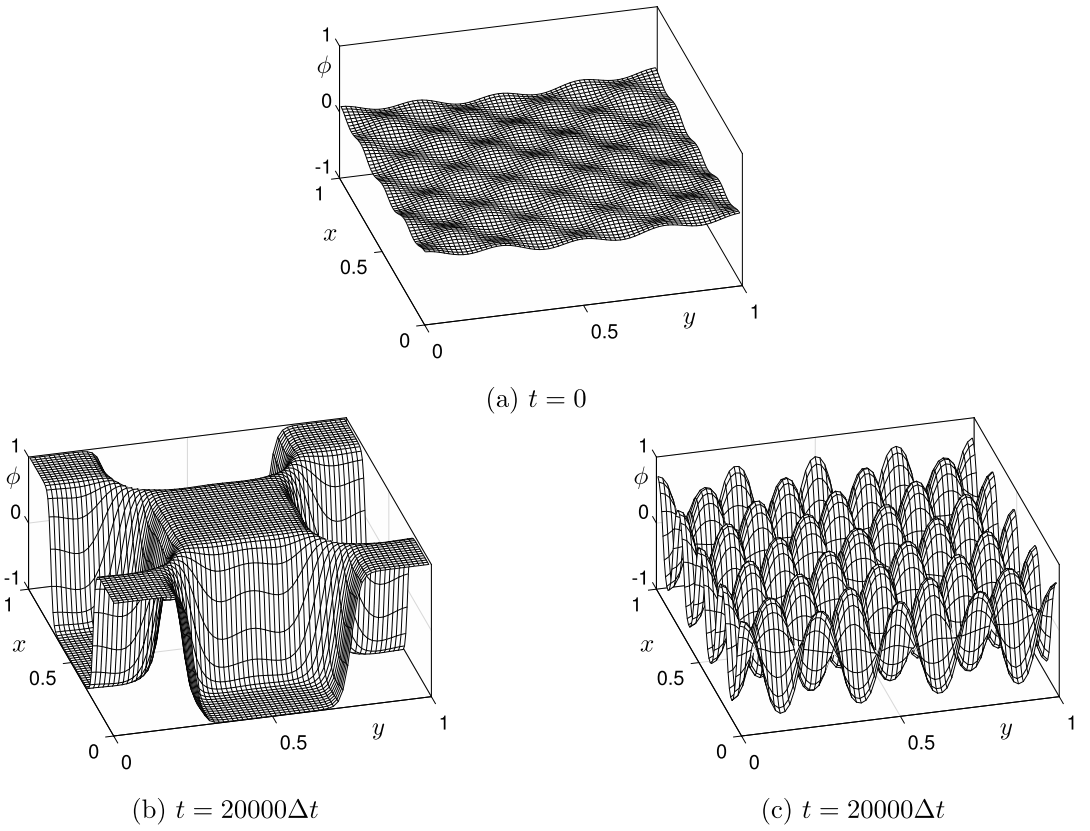

Fig. 8. Temporal evolution of (b) the AC and (c) the CH equations with (a) the initial condition $\phi(x, y, 0) = 0.05\cos(2\pi x)\cos(2\pi y)+0.05\cos(8\pi x)\cos(8\pi y)$.

3.2. Comparison of temporal evolutions

In this section, we compare the numerical results of the AC and the CH equations with respect to initial frequency mode.

3.2.1. One-dimensional space

Based on the linear stability test in one-dimensional space $\Omega = (0, 1)$, we know that the AC and the CH equations have the fastest growth modes when $k = 2$ and $k = 12$, respectively (see Fig. 2).

First, we implement two experiments with the initial conditions (circle marker) set to low and high frequency modes. In Fig. 5, (a) and (b) represent the temporal evolution of the AC and the CH equations, respectively. Also, the first and second columns show the numerical results when $\phi(x, 0) = 0.01\cos(2\pi x)$ and $\phi(x, 0) = 0.01\cos(12\pi x)$, respectively. Here, we use the total time $T = 10000\Delta t$ and $T = 40000\Delta t$ for the AC and the CH equations, respectively. Based on the numerical results, we can observe that the numerical solution of the AC equation grows quickly when $k = 2$, while the CH equation grows when $k = 12$.

To investigate the outcome of combining the initial condition with low and high modes, we perform two numerical tests. We first consider the initial condition as $\phi(x, 0) = 0.01[\cos(2\pi x)+\cos(12\pi x)]$. Fig. 6(a) shows the temporal evolution of the AC equation until $T = 8000\Delta t$. The numerical solution leaves only $k = 2$ mode and the high mode ($k = 12$) disappears over time. On the other hand, the CH equation has a different behavior to the AC equation as shown in Fig. 6(b). Since the fastest mode of the CH equation is $k = 12$, the numerical solution of this equation only has a high mode without low-frequency modes.

Fig. 7 shows the temporal evolution of the AC and the CH equations with $\phi(x, 0) = 0.05\text{rand}(x)$. Here, rand($x$) denotes a random number between -1 and 1. As expected, the numerical result of the AC equation forms relatively few frequency modes compared to the CH equation.

3.2.2. Two-dimensional space

In two-dimensional space $\Omega = (0, 1) \times (0, 1)$, we simulate the numerical test with the initial condition $\phi(x, y, 0) = 0.05\cos(2\pi x)\cos(2\pi y) + 0.05\cos(8\pi x)\cos(8\pi y)$ as shown in Fig. 8(a). Here, $k = 2$ and $k = 8$ are the fastest growth modes of the AC and the CH equations in two-dimensional space, respectively. Similar to the one-dimensional test, the numerical solution of the AC equation grows faster than that of the CH equation, leaving only a low frequency mode.

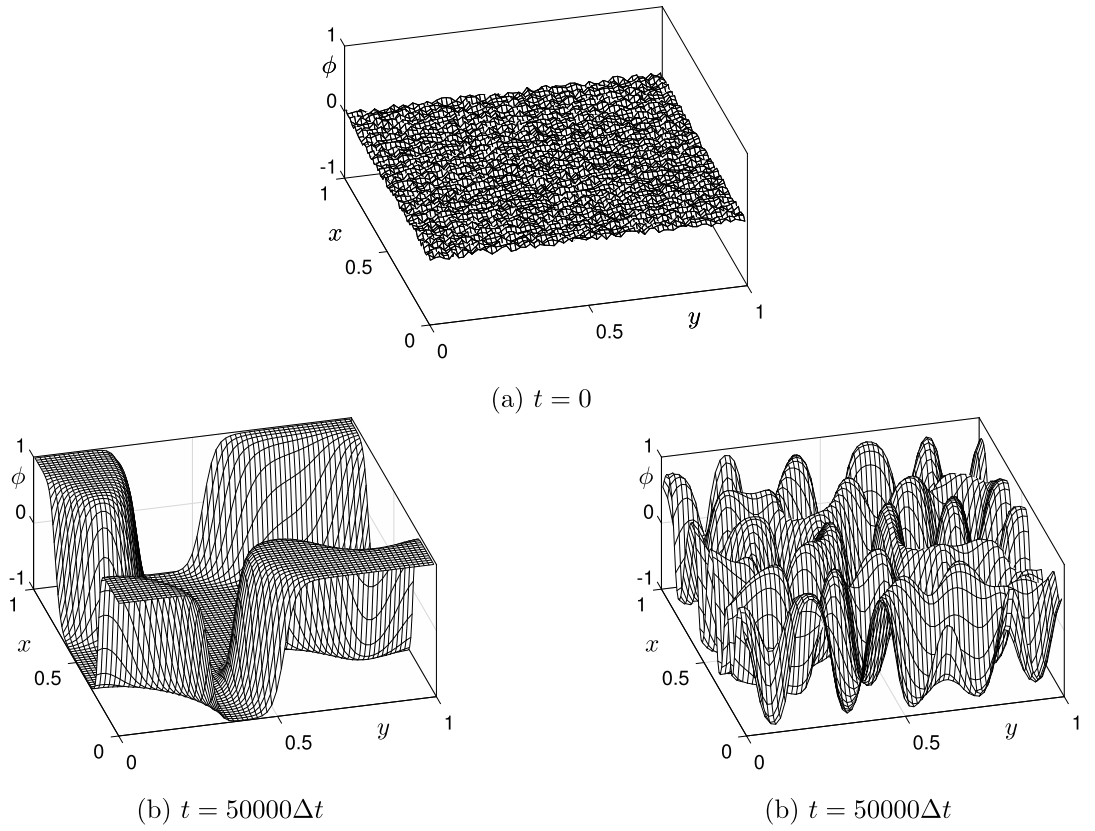

Fig. 9. Temporal evolution of (b) the AC and (c) the CH equations with (a) the initial condition $\phi(x, y, 0) = 0.05\text{rand}(x, y)$. Here, rand$(x, y)$ denotes a random number between -1 and 1.

Next, we consider the initial condition with random perturbation as $\phi(x, y, 0) = 0.05\text{rand}(x, y)$. Here, rand$(x, y)$ denotes the random number between -1 and 1. As shown in Fig. 9, the AC equation has a low frequency mode over time unlike the CH equation.

3.2.3. Three-dimensional space

Now, we examine the same tests in three-dimensional space $\Omega = (0, 1) \times (0, 1) \times (0, 1)$. Fig. 10 represents the isosurface of the numerical solution at the zero level for the AC and the CH equations with the initial condition $\phi(x, y, z, 0) = 0.1\cos(2\pi x)\cos(2\pi y)\cos(2\pi z) + 0.1\cos(6\pi x)\cos(6\pi y)\cos(6\pi z)$.

With the progression of time, the numerical solutions of the AC and CH equations exhibit low and high frequency modes, respectively.

In Fig. 11, we can compare the AC and the CH equations with the random perturbed initial condition as $\phi(x, y, z, 0) = 0.05\text{rand}(x, y, z)$. Here, rand$(x, y, z)$ denotes a random number between -1 and 1. Similarly, the isosurfaces of two equations at the zero level show the same results as the previous tests.

Interestingly, we found a similar dynamics between the two equations for the relaxation of the curved interface. The initial condition is set to

$$\phi(x, y, 0) = \tanh\left(\frac{y - a}{\sqrt{2}\epsilon}\right) + \tanh\left(\frac{b - y}{\sqrt{2}\epsilon}\right) - 1, \tag{20}$$

where $a = 0.25 + 0.2\cos(4\pi x)$ and $b = 0.75 + 0.2\cos(4\pi x)$. As we observe in Fig. 12, it is possible to determine the dynamics of the interface that are almost identical. Note that in Fig. 12, we plot the filled contours, i.e., the phase-field is positive for the shaded region and is negative in the other region. The symbols are at the interface. Therefore, the vertical axis is not ϕ but the y-axis. In this numerical experiment, we do not consider the growth of the phase-field, but instead consider the interface relaxation dynamics. It can be seen in Fig. 12 that there is a time difference. This is due to the fact that the interface in the AC equation moves according to the motion by mean curvature [1,7,8] and the interface in the CH equation moves according to the Mullins–Sekerka evolution, see [31] and references therein for more details.

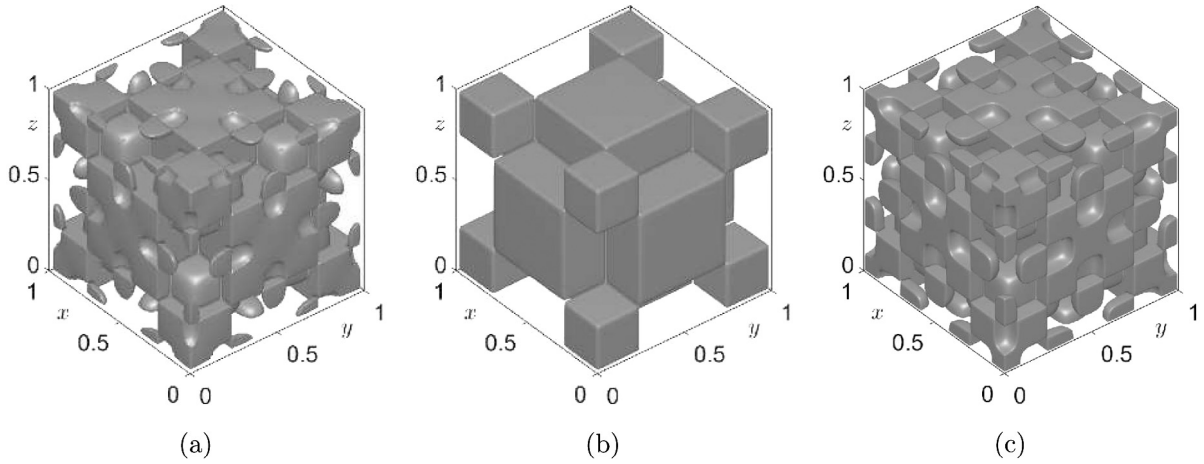

Fig. 10. (a) Initial condition $\phi(x, y, z, 0) = 0.1\cos(2\pi x)\cos(2\pi y)\cos(2\pi z) + 0.1\cos(6\pi x)\cos(6\pi y)\cos(6\pi z)$ and numerical solution of (b) the AC and (c) the CH equations at $T = 10000\Delta t$.

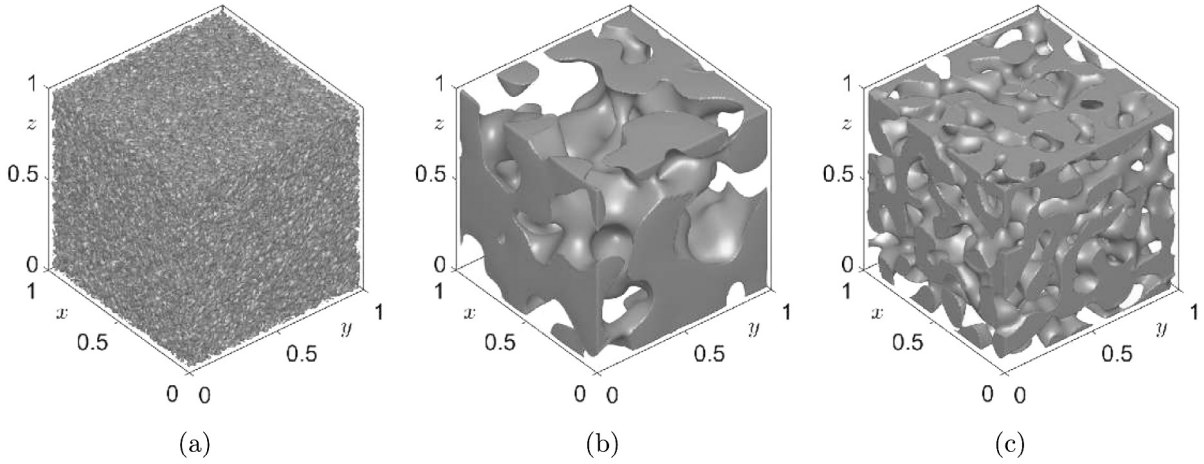

Fig. 11. (a) Initial condition $\phi(x, y, z, 0) = 0.05\text{rand}(x, y, z)$ and numerical solution of (b) the AC and (c) the CH equations at $T = 10000\Delta t$. Here, rand(x, y, z) denotes a random number between -1 and 1.

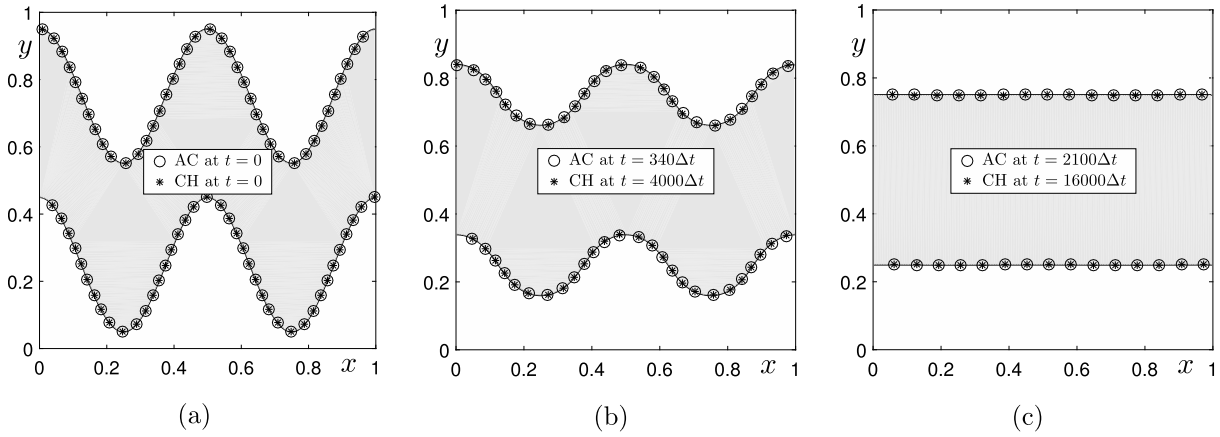

Fig. 12. Temporal evolution of the AC and the CH equations with the initial condition (20) in two-dimensional space $\Omega = (0, 1) \times (0, 1)$.

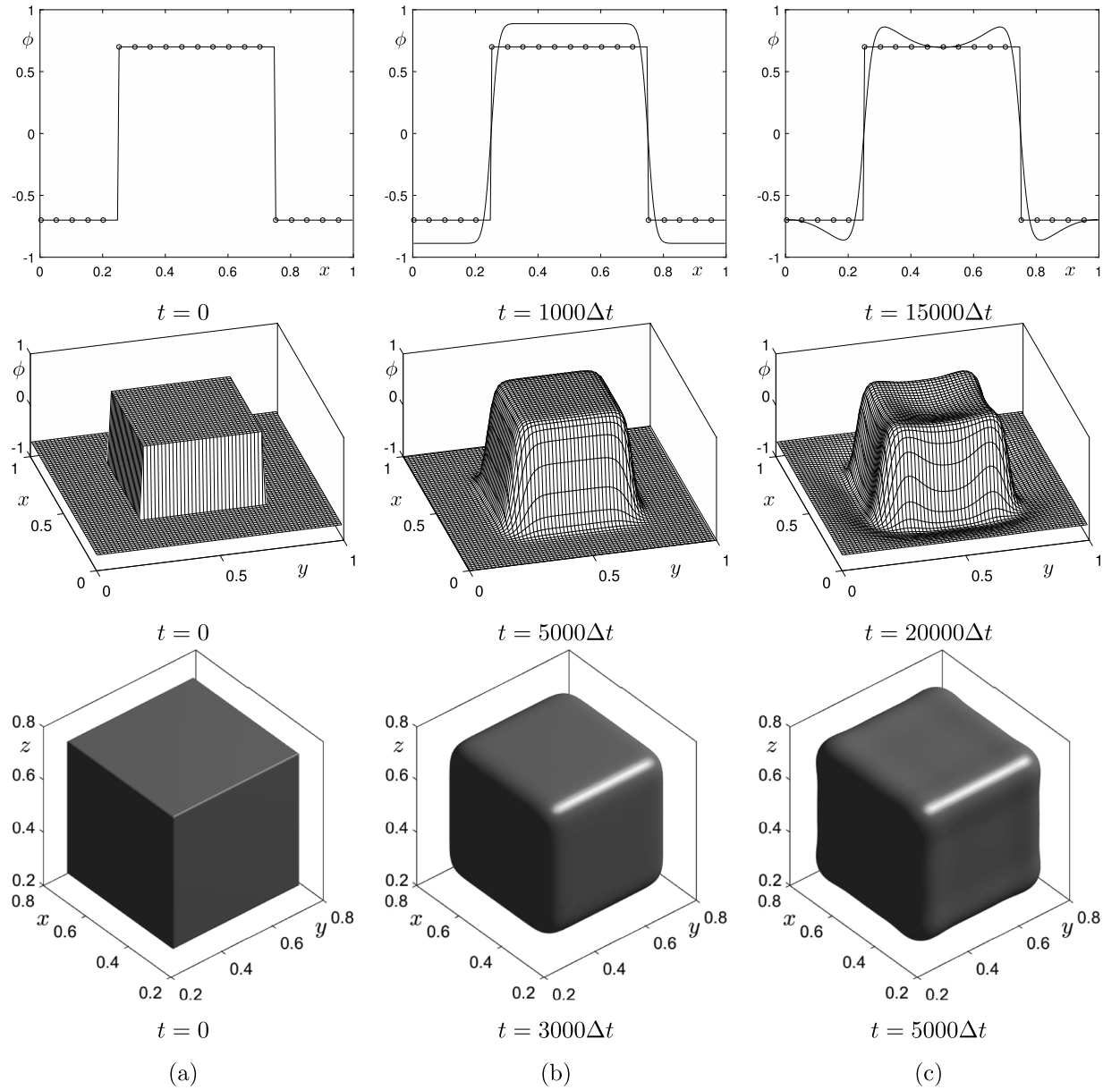

Fig. 13. Column (a) is the step initial condition. Columns (b) and (c) are snapshots of the numerical solutions of the AC and the CH equations at time t. The times are shown below each figure.

3.2.4. Numerical experiment of the AC and the CH equations with step initial conditions

Finally, we perform a numerical experiment of the AC and the CH equations with step initial conditions. The initial conditions are given as:

$$\phi(\mathbf{x}, 0) = \begin{cases} 0.7 & \text{if } \|\mathbf{x} - 0.5\|_\infty \le 0.25, \\ -0.7 & \text{otherwise,} \end{cases}$$

where $\mathbf{x} \in \mathbb{R}^d$ and $d = 1,\ 2$, and 3. Here, the maximum norm is defined as $\|\mathbf{x}\|_\infty = \max_{1 \le i \le d} |x_i|$.

Fig. 13(a), (b), and (c) show the step initial conditions, snapshots of the numerical solutions of the AC and the CH equations at time t, respectively. In the case of the AC equation, the phase-field in the flat region approaches the equilibrium values, i.e., ± 1. However, in the case of the CH equation, the evolutionary dynamics is different. The phase-field is undergoing separation in the neighborhood of the interface, i.e., zero level set, while the phase-field is not changed in the middle of the flat region at early times. This behavior is partly due to the conservation property of the CH equation.

4. Conclusions

We performed a comparison study on the different dynamics between the AC and the CH equations. Linear stability analysis and numerical simulations demonstrated that while the growth rates are monotonically decreasing with respect to the modes for the AC equation, the growth rates for the CH equation increase and then decrease with respect to the modes. The dynamics of the two equations is different. Therefore, the appropriate equation must be used when a particular phenomenon is modeled.

Acknowledgments

Yibao Li is supported by National Natural Science Foundation of China (No. 11601416, No. 11631012). The corresponding author (Junseok Kim) was supported by Korea University Future Research Grant. The authors thank the reviewers for the constructive and helpful comments on the revision of this article.

References

[1] S.M. Allen, J.W. Cahn, A microscopic theory for antiphase boundary motion and its application to antiphase domain coarsening, Acta Metall. 27 (1979) 1085–1095.
[2] Y. Li, D. Jeong, J.-I. Choi, S. Lee, J. Kim, Fast local image inpainting based on the Allen–Cahn model, Digit. Signal Process. 37 (2015) 65–74.
[3] L. Ma, R. Chen, X. Yang, H. Zhang, Numerical approximations for Allen–Cahn type phase field model of two-phase incompressible fluids with moving contact lines, Commun. Comput. Phys. 21 (2017) 867–889.
[4] T. Takaki, T. Shimokawabe, M. Ohno, A. Yamanaka, T. Aoki, Unexpected selection of growing dendrites by very-large-scale phase-field simulation, J. Cryst. Growth 382 (2013) 21–25.
[5] J. Zhao, Q. Wang, X. Yang, Numerical approximations for a phase field dendritic crystal growth model based on the invariant energy quadratization approach, Internat. J. Numer. Methods Engrg. 110 (3) (2017) 279–300.
[6] D.S. Lee, J.S. Kim, Mean curvature flow by the Allen–Cahn equation, Eur. J. Appl. Math. 26 (4) (2015) 535–559.
[7] X. Feng, A. Prol, Numerical analysis of the Allen–Cahn equation and approximation for mean curvature flows, Numer. Math. 94 (2003) 33–65.
[8] X. Feng, Y. Li, Analysis of symmetric interior penalty discontinuous Galerkin methods for the Allen–Cahn equation and the mean curvature flow, IMA J. Numer. Anal. 35 (2015) 1622–1651.
[9] M. Benes, V. Chalupecky, K. Mikula, Geometrical image segmentation by the Allen–Cahn equation, Appl. Numer. Math. 51 (2004) 187–205.
[10] Y. Li, J. Kim, An unconditionally stable hybrid method for image segmentation, Appl. Numer. Math. 82 (2014) 32–43.
[11] J.W. Cahn, J.E. Hilliard, Spinodal decomposition: a reprise, Acta Metall. 19 (1972) 151–161.
[12] T. Aboelenen, H.M. El-Hawary, A high-order nodal discontinuous Galerkin method for a linearized fractional Cahn–Hilliard equation, Comput. Math. Appl. 73 (6) (2017) 1197–1217.
[13] Y. Li, D. Jeong, J. Shin, J. Kim, A conservative numerical method for the Cahn–Hilliard equation with Dirichlet boundary conditions in complex domains, Comput. Math. Appl. 65 (2013) 102–115.
[14] Y. Li, H.G. Lee, B. Xia, J. Kim, A compact fourth-order finite difference scheme for the three-dimensional Cahn–Hilliard equation, Comput. Phys. Comm. 200 (2016) 108–116.
[15] Y. Li, Y. Choi, J. Kim, Computationally efficient adaptive timestep method for the Cahn–Hilliard equation, Comput. Math. Appl. 73 (8) (2017) 1855–1864.
[16] S. Zhou, M. Wang, Multimaterial structural topology optimization with a generalized Cahn–Hilliard model of multiphase transition, Struct. Multidiscip. Optim. 33 (2) (2007) 89–111.
[17] V.E. Badalassi, H.D. Ceniceros, S. Banerjee, Computation of multiphase systems with phase field models, J. Comput. Phys. 190 (2003) 371–397.
[18] Y. Li, J.-I. Choi, J. Kim, Multi-component Cahn–Hilliard system with different boundary conditions in complex domains, J. Comput. Phys. 323 (2016) 1–16.
[19] Y. Li, J.-I. Choi, J. Kim, A phase-field fluid modeling and computation with interfacial profile correction term, Commun. Nonlinear Sci. Numer. Simul. 30 (2016) 84–100.
[20] M. Kotschote, R. Zacher, Strong solutions in the dynamical theory of compressible fluid mixtures, Math. Models Methods Appl. Sci. 25 (7) (2013) 1217–1256.
[21] A. Bertozzi, S. Esedoglu, A. Gillette, Inpainting of binary images using the Cahn–Hilliard equation, IEEE Trans. Image Process. 16 (2007) 285–291.
[22] Y. Li, J. Shin, Y. Choi, J. Kim, Three-dimensional volume reconstruction from slice data using phase-field models, Comput. Vis. Image Underst. 137 (2015) 115–124.
[23] D. Jeong, J. Shin, Y. Li, Y. Choi, J-H. Jung, S. Lee, J. Kim, Numerical analysis of energy–minimizing wavelengths of equilibrium states for diblock copolymers, Curr. Appl. Phys. 14 (9) (2014) 1263–1272.
[24] M. Maraldi, L. Molari, D. Grandi, A unified thermodynamic framework for modelling of diffusive and displacive phase transitions, Internat. J. Engrg. Sci. 50 (1) (2012) 31–45.
[25] S.M. Wise, J.S. Lowengrub, H.B. Frieboes, V. Cristini, Three–pdimensional multispecies nonlinear tumor growth-I: model and numerical method, J. Theoret. Biol. 253 (3) (2008) 524–543.
[26] J. Zhu, L.Q. Chen, J. Shen, Computer simulation of morphological evolution during phase separation and coarsening with strong inhomogeneous elasticity, Model. Simulat. Mater. Sci. Eng. 9 (6) (2001) 499–511.
[27] J. Shen, T. Tang, L.-L. Wang, Spectral Methods: Algorithms, Analysis and Applications, Vol. 41, Springer Science & Business Media, 2011, pp. 23–46.
[28] D.J. Eyre, http://www.math.utah.edu/~eyre/research/methods/stable.ps.
[29] S. Lee, C. Lee, H.G. Lee, J. Kim, Comparison of different numerical schemes for the Cahn–Hilliard equation, J. KSIAM 17 (3) (2013) 197–207.
[30] J.W. Choi, H.G. Lee, D. Jeong, J. Kim, An unconditionally gradient stable numerical method for solving the Allen–Cahn equation, Physica A 388 (2009) 1791–1803.
[31] R.L. Pego, Front migration in the nonlinear Cahn–Hilliard equation, Proc. R. Soc. Lond. Ser. A Math. Phys. Eng. Sci. 422 (1989) 261–278.